












# Commissioning experiment of the high-contrast SILEX-II multi-petawatt laser facility

Cite as: Matter Radiat. Extremes 6, 064401 (2021); doi: 10.1063/5.0016019

Submitted: 31 May 2020 • Accepted: 15 September 2021 •

Published Online: 6 October 2021



Wei Hong,<sup>1,a)</sup>  Shukai He,<sup>1</sup>  Jian Teng,<sup>1</sup> Zhigang Deng,<sup>1</sup> Zhimeng Zhang,<sup>1</sup> Feng Lu,<sup>1</sup> Bo Zhang,<sup>1</sup> Bin Zhu,<sup>1</sup> Zenghai Dai,<sup>1</sup> Bo Cui,<sup>1</sup> Yuchi Wu,<sup>1</sup> Dongxiao Liu,<sup>1</sup>  Wei Qi,<sup>1</sup> Jinlong Jiao,<sup>1</sup>  Faqiang Zhang,<sup>1</sup> Zuhua Yang,<sup>1</sup> Feng Zhang,<sup>1</sup> Bi Bi,<sup>1</sup> Xiaoming Zeng,<sup>1</sup> Kainan Zhou,<sup>1</sup> Yanlei Zuo,<sup>1</sup> Xiaojun Huang,<sup>1</sup> Na Xie,<sup>1</sup> Yi Guo,<sup>1</sup> Jingqin Su,<sup>1</sup> Dan Han,<sup>1</sup> Ying Mao,<sup>1</sup> Leifeng Cao,<sup>1</sup> Weimin Zhou,<sup>1</sup> Yuqiu Gu,<sup>1</sup>  Feng Jing,<sup>1</sup> Baohan Zhang,<sup>1</sup> Hongbo Cai,<sup>2</sup>  Mingqing He,<sup>2</sup> Wudi Zheng,<sup>2</sup> Shaoping Zhu,<sup>2</sup> Wenjun Ma,<sup>3</sup>  Dahui Wang,<sup>3</sup>  Yinren Shou,<sup>3</sup>  Xueqing Yan,<sup>3</sup>  Bin Qiao,<sup>4</sup> Yi Zhang,<sup>4</sup>  Congling Zhong,<sup>4</sup>  Xiaohui Yuan,<sup>5</sup> and Wenqing Wei<sup>5</sup>

## AFFILIATIONS

<sup>1</sup>Science and Technology on Plasma Physics Laboratory, Laser Fusion Research Center, CAEP, Mianyang, Sichuan Province 621900, China

<sup>2</sup>Institute of Applied Physics and Computational Mathematics, Beijing 100871, China

<sup>3</sup>Institute of Heavy Ion Physics, Peking University, Beijing 100871, China

<sup>4</sup>School of Physics, Peking University, Beijing 100871, China

<sup>5</sup>School of Physics and Astronomy, Shanghai Jiao Tong University, Shanghai 200240, China

<sup>a)</sup> Author to whom correspondence should be addressed: [jminhong@126.com](mailto:jminhong@126.com)

## ABSTRACT

The results of a commissioning experiment on the SILEX-II laser facility (formerly known as CAEP-PW) are reported. SILEX-II is a complete optical parametric chirped-pulse amplification laser facility. The peak power reached about 1 PW in a 30 fs pulse duration during the experiment. The laser contrast was better than  $10^{10}$  at 20 ps ahead of the main pulse. In the basic laser foil target interaction, a set of experimental data were collected, including spatially resolved x-ray emission, the image of the coherent transition radiation, the harmonic spectra in the direction of reflection, the energy spectra and beam profile of accelerated protons, hot-electron spectra, and transmitted laser energy fraction and spatial distribution. The experimental results show that the laser intensity reached  $5 \times 10^{20}$  W/cm<sup>2</sup> within a 5.8  $\mu$ m focus (FWHM). Significant laser transmission did not occur when the thickness of the CH foil was equal to or greater than 50 nm. The maximum energy of the accelerated protons in the target normal direction was roughly unchanged when the target thickness varied between 50 nm and 15  $\mu$ m. The maximum proton energy via the target normal sheath field acceleration mechanism was about 21 MeV. We expect the on-target laser intensity to reach  $10^{22}$  W/cm<sup>2</sup> in the near future, after optimization of the laser focus and upgrade of the laser power to 3 PW.

© 2021 Author(s). All article content, except where otherwise noted, is licensed under a Creative Commons Attribution (CC BY) license (<http://creativecommons.org/licenses/by/4.0/>). <https://doi.org/10.1063/5.0016019>

## I. INTRODUCTION

The invention and application of the chirped pulse amplification technique in short-pulse lasers has led to unprecedented ultra-high laser peak powers.<sup>1</sup> After more than three decades of development, petawatt ( $10^{15}$  W) class lasers, with pulse durations varying from a few femtoseconds to several picoseconds, have been constructed around the world.<sup>2,3</sup> The focused laser intensity reaches as high as  $10^{22}$  W/cm<sup>2</sup>.<sup>4,5</sup> Recently, several new femtosecond laser facilities have demonstrated output laser powers of up to 10 PW.<sup>3,6</sup> A new facility, the Station of

Extreme Light Science (SEL), which aims to produce 100 PW laser pulses in 2023, is under construction in Shanghai, China. Not only do these ultra-intense lasers have many applications, such as high-energy ion acceleration, laser electron wakefield acceleration, ultrafast x-rays, and fast ignition, with their increased intensity, they will also bring new fundamental research opportunities in areas such as strong-field quantum electrodynamics.<sup>7</sup>

The first multi-hundred terawatt laser (SILEX-I) started operation at the Laser Fusion Research Center, CAEP in 2004.<sup>8</sup> This first

high-peak-power laser facility was followed by an even larger-scale laser facility, Xingguang-III, which is capable of generating three synchronized laser pulses of femtosecond, picosecond, and nanosecond pulse durations.<sup>9</sup> In 2016, the construction of the third ultra-high-power laser facility, SILEX-II, of 4.9 PW power and 18.6 fs duration, was completed.<sup>10,11</sup> Besides the extremely high peak power of SILEX-II, its temporal contrast reaches higher levels, thanks to the employment of the complete optical parametric chirped-pulse amplification (OPCPA) technique. The temporal contrast is better than  $10^{10}$  at 20 ps before the main pulse. In 2018, a commissioning experiment was carried out on this high-contrast high-intensity laser facility. A set of experimental results was obtained with an on-target laser power around 1 PW. These results are correlated with the laser focus, temporal contrast, and laser intensity. The confirmed laser parameters in the commissioning experiment provide a solid basis for future laser–target interaction experiments and the optimization of the laser facility.

The commissioning experiment focused on the characterization of laser–plane foil interaction. A set of comprehensive diagnostics were set up around the target to collect the spatially resolved x-ray emission, the image of the coherent transition radiation (CTR), the harmonic spectra in the direction of reflection, the energy spectra and beam profile of accelerated protons, hot-electron spectra, and transmitted laser energy fraction and spatial distribution. From the complete experimental dataset, the on-target laser spot size, laser intensity, and prepulse level can be inferred. The data suggest that the laser intensity reaches  $5 \times 10^{20}$  W/cm<sup>2</sup> with a 5.8  $\mu$ m focus (FWHM) and 30 fs pulse duration. The laser is of inherent high temporal contrast owing to the complete OPCPA technique. When the S-polarized laser pulse impinged on the CH foil at 30° with respect to the target normal, relativistic transparency occurred for a foil of thickness 20 nm. The cutoff energy of the proton beams accelerated by standard target normal sheath field acceleration (TNSA) was almost independent of the target thickness when this varied between 50 nm and 15  $\mu$ m. The maximum proton energy was about 21 MeV in the target normal direction.

## II. TARGET AREA AND LASER PARAMETERS

The detailed design, structure, parameters, and performance of SILEX-II laser facility have been reported previously.<sup>10,11</sup> The central wavelength of the laser is 800 nm. The repetition rate is one shot every 5 min for preamplifier output (50 mJ on targets) and 1 shot per hour for the full output (30 J on targets), respectively. The shortest pulse duration is 18.6 fs. The pulse duration was measured with a single-shot autocorrelator, by applying a Gaussian deconvolution factor. Both the entire beam and a sampling portion have been used to characterize the pulse duration, and it has been found that there is little difference between the two cases. The laser contrast measured by a single-shot third-order autocorrelator can be found in Fig. 7 of Ref. 10. The temporal contrast at 20 ps before the main pulse reaches  $10^{10}$ , which is the measurement limit of the autocorrelator. The obvious change in temporal contrast within 20 ps before the main pulse is mainly attributed to optical parametric fluorescence and spectral-phase distortion. The near field of the final laser beam is an eighth-order super Gaussian and the measured modulation is about 1.8. The large modulation is largely due to the large modulation of the pump laser beam for the main amplifier.

In the commissioning experiment, the maximum laser energy on target was 32.6 J due to a smaller LBO crystal used in the main amplifier, although the demonstrated highest energy of the compressed laser pulse of SILEX-II is 91.9 J.<sup>10</sup> The laser energy on targets was  $27 \pm 2.7$  J (rms), and the laser pulse duration was  $34.5 \pm 2.5$  fs (rms) for the total of 30 shots.

Figure 1 is a photograph of the target area of the SILEX-II laser facility. The three vacuum chambers are the deformable mirror chamber, the laser–target interaction chamber containing the short-focus parabola, and the chamber for the long-focus parabola. Only the short-focus parabola ( $f = 800$  mm) was used in the commissioning experiment. The whole target area is surrounded by specially designed radiation-shielding walls.

Figure 2 shows the structure of the laser–target interaction chamber and the laser path inside the chamber. The laser beam from the deformable mirror chamber is reflected by the turning mirror  $M_1$  to the on-axis parabola  $P_1$ . The converging laser beam from  $P_1$  passes through a 68 mm circular hole in the center of  $M_1$  and focuses at a point about 5 cm from the rear side of  $M_1$ . The cross section of the laser beam is a  $220 \times 210$  mm<sup>2</sup> rectangle and the effective F-number is 2.63 for the 800 mm focal length parabola. An image system with an F/1.4 lens is used to measure the laser focus in the vacuum chamber. Even though the space before the target is very limited for diagnoses in the experiment, the on-axis parabola is more easily aligned than the off-axis parabola. In addition, the secondary laser beam through the hole in  $M_1$  can be used for on-site measurement of laser parameters.

In high-field experiments, precise data on the laser focus is essential for laser–target interaction. The quality of laser focus is a critical factor in determining the laser intensity. Figure 3 shows the measured laser focus with the laser light from the preamplifier of SILEX-II for a laser energy of 50 mJ.

A laser focus of this relatively high quality was obtained after correction of the laser wave front with the deformable mirror. The deformable mirror consists of 49 ( $7 \times 7$ ) elements. During the process of wavefront correction, a wavefront sampling lens was installed after the focusing parabola so that the aberration of the focusing parabola could also be corrected. The intensity distribution of the laser focus



FIG. 1. Target area of SILEX-II laser facility.

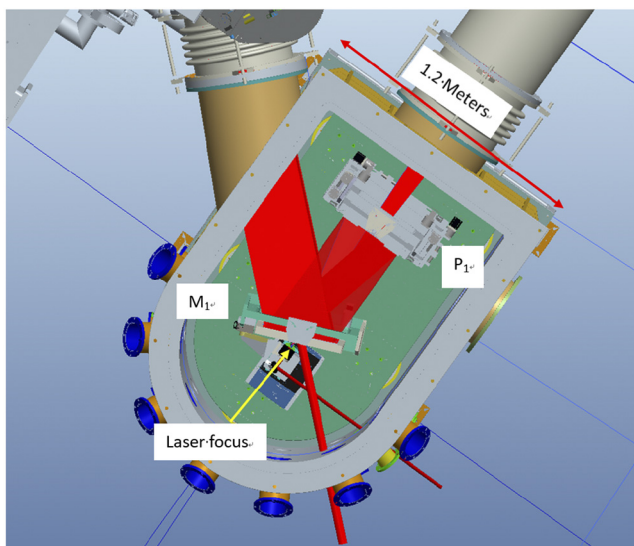


**FIG. 2.** Top view of laser–target interaction chamber containing the short–focus parabola.

can be fitted by a Gaussian function with an FWHM of  $5.4 \mu\text{m}$ . Seventeen percent of the laser energy was contained within the  $5.4 \mu\text{m}$  circular spot. The size of the ideal Airy spot should be  $2.2 \mu\text{m}$  (FWHM), containing 80% of the laser energy for the current focusing system. Also, owing to the relatively large aberration resulting from the current focus system, the observed far field (see Fig. 3) actually looks more like a circle than the rectangle that would be expected for an ideal rectangular laser beam.

The far field shown in Fig. 3 was measured for a laser energy of 50 mJ instead of the full laser energy of 30 J. This is because direct measurement of the far field is very challenging owing to the risk of

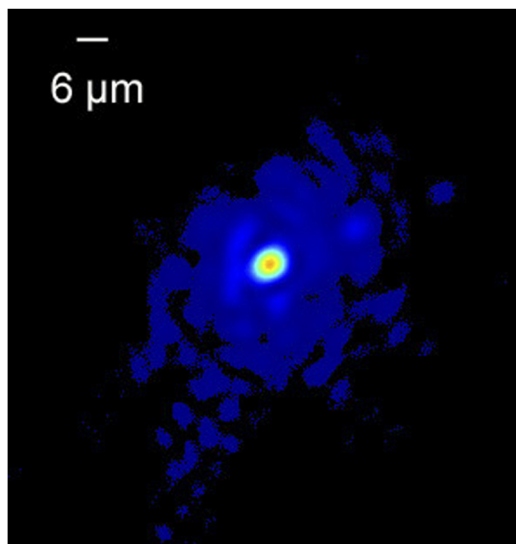


**FIG. 3.** Laser focus of SILEX-II with an F/2.6 on-axis parabola.

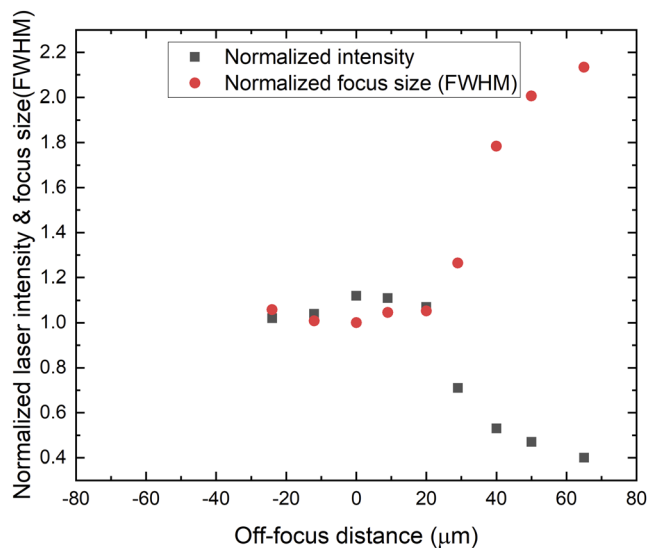


**FIG. 4.** Dependence of laser focus parameters on off-focus distance, obtained using laser light from an oscillator (77 MHz, 5 mW).

damage by high-power laser radiation. Instead, to explore the properties of the laser focus under high-laser-energy conditions, the near field for a full laser energy of 30 J was measured. It was found that the near field exhibits an eighth-order super-Gaussian profile with a modulation of about 1.8, and so the intensity distribution across the beam is nearly flat. Both the near and far fields are believed to change with the laser energy, especially in the range from 50 mJ to 30 J. However, the measured laser focus at low laser energies can still provide a reference for the focus at high energies.

Figure 4 shows the dependence of the laser spot parameters on the off-focus distance, obtained using laser light from an oscillator (77 MHz, 5 mW). The laser intensity and focus size (FWHM) are normalized by their values at the focus. The laser intensity distribution of the central spot is similar for all off-focus distances less than  $\pm 20 \mu\text{m}$ . The laser intensity drops to about half of its maximum at a position  $35 \mu\text{m}$  from the focus, which is consistent with the expected  $39 \mu\text{m}$  Rayleigh length for the F/2.6 focusing system. When the off-focus distance reaches  $65 \mu\text{m}$ , distortion of the central bright spot appears, and the laser intensity drops to 29% of its maximum. During the experiment, the targets were aligned within  $\pm 20 \mu\text{m}$  from the focus, and the decrease of the laser intensity from its maximum was less than 10%.

Based on the focus data, the laser intensity was  $4.7 \times 10^{20} \text{ W/cm}^2$  within FWHM for 1 PW laser power.

### III. EXPERIMENTAL RESULTS AND DISCUSSION

#### A. Experimental setup

In the commissioning experiment, the S-polarized laser impinged on plane foils at  $30^\circ$  or  $0^\circ$ . A set of diagnostic instruments were installed in the horizontal plane (Fig. 5). An Ocean HR2000+ optical spectrometer was set up to measure the reflected laser light at about  $40^\circ$  with respect to the target normal. An electron spectral meter (4000 G static magnetic field) was used to measure the electron spectra emitted from



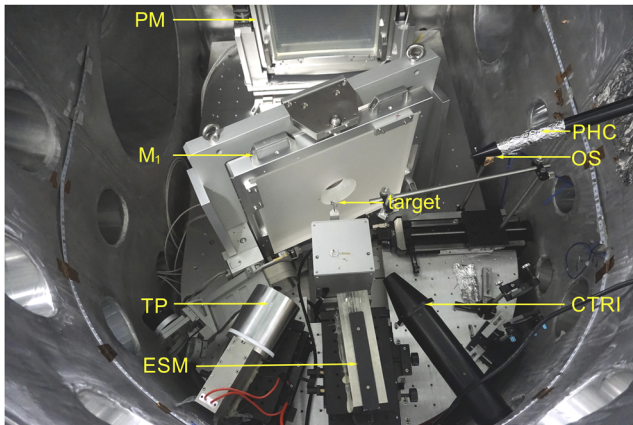


**FIG. 5.** Interior of the interaction chamber with the installed diagnostics. TP, Thompson spectrometer; ESM, electron spectral meter; OS, Ocean HR2000+ optical spectrometer; PHC, x-ray pinhole camera; CTRI, coherent transition radiation imager; PM, parabola;  $M_1$ , turning mirror.

the target rear side in the laser propagation direction. A piece of radiochromic film (RCF) (HD-V2) was used to measure the transmitted laser beam through the thin foils. A Thompson spectrometer and a stack of RCFs were used to measure the ion spectra and proton beam profile in the target normal direction behind the target. A high-resolution optical imaging system, with a working wavelength of 400 nm, was employed to take a picture of the coherent transition radiation from the rear side of the target at an angle of  $60^\circ$  from the target normal. In addition, an x-ray pinhole camera located above the horizontal plane was used to obtain an image of x-rays at an energy of about 1 keV.

## B. Experimental results related to basic laser parameters

### 1. Experimental results related to laser focus

For large-scale laser facilities, reports of direct optical laser focus measurements under full energy output conditions are rare. However,

Pirozhkov *et al.*<sup>5</sup> have made some important progress and reported the  $1.3 \mu\text{m}$  (FWHM) laser focus on the J-KAREN-P laser facility, where the 20 J laser energy was attenuated by orders of magnitude by using 10 optical wedges. So far, for the SILEX-II facility, as pointed out in Sec. II, even though the laser focus is measured in the interaction chamber, the laser light used in the measurement is from the preamplifier when the main amplifier is not pumped-on. Theoretically, the focus should be almost the same for the two cases when the main amplifier is on and when it is off for the OPCPA laser, but this expectation has not yet been confirmed by direct optical measurement. Therefore, in the commissioning experiment, x-ray pinhole imaging and coherent transition radiation imaging were used to diagnose the laser focus when a laser pulse of full energy (about 30 J) impinged on the targets.

Figure 6(a) is a typical x-ray image taken by the x-ray pinhole camera. The pinhole was  $17 \mu\text{m}$  in diameter and was covered by a  $20 \mu\text{m}$  thick beryllium foil. The magnification of the pinhole camera was 3.2. The target was a piece of  $2 \mu\text{m}$  thick Cu foil. The size (FWHM) of the circular bright x-ray spot in Fig. 6(a) is  $56 \times 53 \mu\text{m}^2$ . Generally, x-ray spots are much larger than the laser focus. The x-ray pinhole camera can roughly resolve the structure of x-ray images even though its hole size is larger than the laser focus. For example, in an abnormal shot as shown in Fig. 6(b), the on-target laser intensity distribution is distorted so much that even the x-ray pinhole camera can resolve the complex structure of the x-ray image. In this case, the x-ray intensity is one-third of normal intensity, the image is larger and scattering, and the measured hot-electron temperature and cutoff energy of accelerated protons are lower, which suggests the laser intensity is lower in this shot. Unexpected modulation of the spectral phase may be the reason for the abnormal shot shown in Fig. 6(b).

Compared with the x-ray pinhole imaging technique, the coherent transition radiation imaging technique can achieve much higher spatial resolution in diagnosis of the laser focus in high-intensity short-pulse laser interaction experiments if certain experimental conditions are met. Coherent transition radiation (CTR) in intense short-pulse laser–target interactions has been widely studied.<sup>12–15</sup> Figure 7(a) is a schematic of the generation of CTR in laser–foil interaction under normal-incidence, high-laser-contrast conditions. When the high-intensity laser pulse impinges steeply

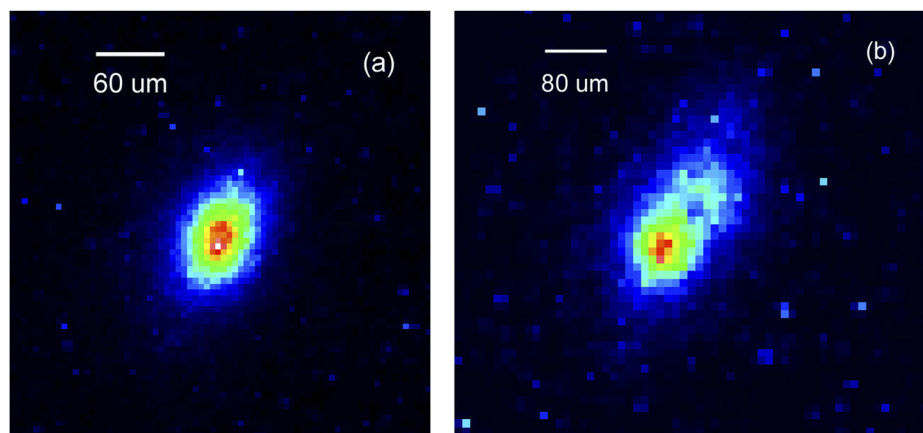


**FIG. 6.** Images taken by the x-ray pinhole camera: (a) normal shot for a laser energy of 29.8 J; (b) abnormal shot for a laser energy of 28.9 J.

on the dense plasma surface, a train of electron bunches with velocity close to that of light is produced via the  $\mathbf{J} \times \mathbf{B}$  mechanism within the laser focus and propagates forward. The distance between relativistic electron bunches is equal to half the wavelength of the incident laser. When these periodic hot electrons pass through the boundary between the target rear side and the vacuum, a pulse of electromagnetic radiation of wavelength half that of the incident laser is emitted into the vacuum. This radiation is well known as CTR. Three experimental conditions must be met to employ CTR imaging to diagnose laser focus. First, the laser contrast must be high enough to avoid the formation of a large-scale preplasma. Filamentation or self-focusing of the laser beam in a large-scale preplasma would make the laser spot on the critical surface very different from that in vacuum, and the CTR image would not represent the original laser focus in vacuum. Second, the laser pulse must impinge normally on the target surface. Intense sheath fields ( $>10^{12}$  V/m) grow rapidly on both front and rear surfaces of a foil target when the target is irradiated by an intense short laser pulse. Multiple reflux of the hot-electron beam will occur between the front and rear surfaces owing to these sheath fields. If the laser pulse impinged obliquely on the foil surface, the multiple reflux would lead to an increase in size of the CTR image in the dimension parallel to the plane of incidence of the laser. Therefore, the temporally integrated CTR image would be distorted from a circular one to an ellipse. Third, the thickness of the foil target must be considerably smaller than the size of the laser focus. The typical divergent angle of the electron beam produced on the target front surface is a few tens of degrees. A thick target would lead to significant increase in the transverse size of the hot-electron beam, and the CTR spot size would be substantially larger than the original laser focus. In addition, the propagation of an extremely high-current electron beam in a high-density target is very complicated, and therefore, to avoid the occurrence of complex hot-electron patterns, thick foils should not be used.

In the commissioning experiment, CTR images were taken when these three requirements were almost satisfied. The target was a  $2 \mu\text{m}$  thick Cu foil, which was normally irradiated by the laser pulse. The scale length of the preplasma was only  $0.3 \mu\text{m}$  according to a 2D hydrodynamic simulation based on the measured prepulse. The spatial resolution of the coherent transition radiation imager (CTRI) was  $3 \mu\text{m}$ . Figure 7(b) shows a typical CTR image for 400 nm

wavelength light. The size (FWHM) of the central bright spot in Fig. 7(b) is  $6.7 \times 7.0 \mu\text{m}^2$ , which is  $1.4 \mu\text{m}$  larger than the expected laser focus ( $5.4 \mu\text{m}$ ). From this result, the estimated divergent angle of the hot-electron beam is about  $20^\circ$ , which agrees with the general expectation. This measurement confirms that the laser spot is smaller than  $7 \mu\text{m}$  under the full-energy laser–target interaction condition.

## 2. Experimental results related to laser contrast

Laser contrast plays a significant role in high-intensity laser–plasma interaction. Two diagnostics are used to characterize the contrast of the SILEX-II laser. The first is the intensity of the three-halves harmonic emitted from a plane target in the direction close to reflection. The second is the laser transmittance through a few tens of nanometers thick ultrathin foils.

It is well known that a three-halves harmonic is generated by a two-plasmon decay (TPD) process in the region of plasma density close to one-quarter of the critical density. It has been shown that the intensity of this three-halves harmonic is strongly dependent on the density scale length at one-quarter critical density.<sup>16</sup> As shown in Fig. 4 of Ref. 16, only when the density scale length at one-quarter critical density is larger than the laser wavelength will the three-halves harmonic appear. When the plasma density scale length at one-quarter critical density increases to about twice the laser wavelength, the intensity of the three-halves harmonic rapidly increases to saturation and then decreases gradually with further increase in scale length. To estimate the density scale length of the plasma formed by the laser prepulse in the commissioning experiment, a 2D hydrodynamic simulation using the XRL2D code was performed. The prepulse data was from Ref. 10, and the target was a  $2 \mu\text{m}$  thick Al foil. Figure 8(a) shows the preplasma density profile along the target normal from the simulation, and it can be seen that the density scale length at one-quarter critical density is  $0.35 \mu\text{m}$  (i.e., 0.44 wavelength). Figure 8(b) shows the measured reflected spectra for three shots. In the two regular shots (red and blue curves), the three-halves harmonic is barely visible. On the contrary, when an extra prepulse is intentionally applied, a much stronger three-halves harmonic (black curve) appears. The experimental results agree with the 2D hydrodynamic simulation, showing that the scale length at one-quarter critical density was small

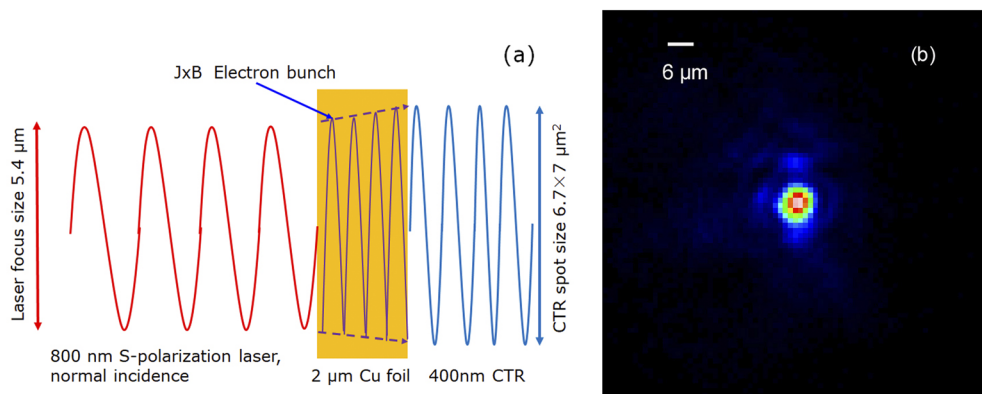
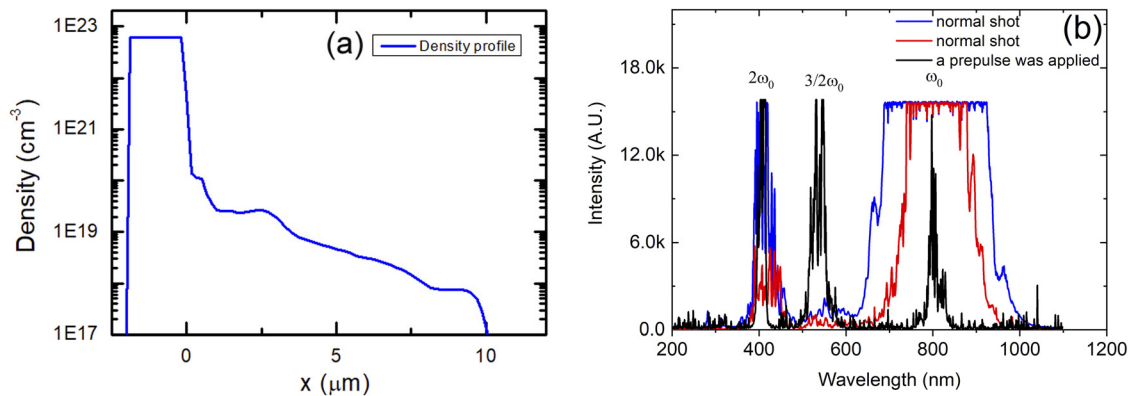


FIG. 7. (a) Schematic of diagnosis of laser focus by coherent transition radiation (CTR). (b) Image of CTR at 400 nm; the size (FWHM) of the central spot is  $6.7 \times 7.0 \mu\text{m}^2$ .



**FIG. 8.** (a) Plasma density profile of the preplasma along the target normal from the XRL2D hydrodynamic simulation for a  $2\ \mu\text{m}$  thick Al foil. (b) Reflected spectra from  $2\ \mu\text{m}$  thick copper foil targets. An extra prepulse was applied on purpose when the black curve was measured.

(less than twice the laser wavelength) owing to the inherent high contrast of the complete OPCPA laser.

The setup for the laser-ultrathin foil interaction experiment is shown in Fig. 9(a). The laser is S-polarized, and the incident angle is  $30^\circ$ . The typical accelerated proton beam via the TNSA mechanism is emitted in the target normal direction, and the transmitted laser goes roughly along the incident laser direction. A large piece of RCF (HD-V2) is installed at a position 28 cm away from the target and is used for measurement of the transmitted laser. Calibration of the quantitative response of the HD-V2 RCF to a femtosecond laser was carried out separately.<sup>17</sup> The calibration shows the clear colorization of the RCF when the laser flux goes beyond the threshold ( $\sim 2\ \text{mJ}/\text{cm}^2$ ). Furthermore, the change in the optical density of the RCF is directly proportional to the laser flux. With the calibration data, a quantitative measurement of the transmitted laser beam with high spatial resolution can be achieved.

In two successive experimental shots, the RCFs were used to measure the transmitted laser beam through 20 nm thick and 50 nm thick CH foils, respectively. The results are shown in Figs. 9(c) and 9(d). The laser pulse duration was 33 fs for both shots. The on-target laser energy was 27.7 and 29.6 J, respectively. The white spots in Figs. 9(c) and 9(d) overlap with the center of the laser beam. The red dashed square in Fig. 9(c) indicates the expected area of impingement of the laser beam on the RCF if the laser propagates in vacuum. The RCF was intentionally left uncovered except in the irregular blue polygonal area in Fig. 9(c), where it was covered by a  $25\ \mu\text{m}$  thick Al foil, which completely blocked the transmitted laser. The irregular red polygon in Fig. 9(d) indicates the area where the RCF was blocked by other installed instruments.

Generally, as well as ultra-short-pulse lasers, RCFs are also sensitive to energetic ions, electrons, and x-rays. Separation of the response of the RCF to the laser from its response to other radiation is not always possible. However, by taking advantage of the experimental setup shown in Fig. 9(a) and by analyzing the experimental results, we succeeded in measuring the transmitted laser beam by subtracting the colorization of the RCF due to energetic ions, electrons, and x-rays.

Compared with Fig. 9(d) (50 nm CH case), the most outstanding feature of Fig. 9(c) (20 nm CH case) is the significant colorization of the filamentary structure within the area outlined by the black dashed square. The shape of this area of significant colorization can be

considered to be square, even though the complete area of significant colorization was not obtained. The square shape of the significant colorization completely excludes the possibility of energetic ions, electrons, and x-rays as sources of this colorization, because their transverse sections of these beams could not be squares. On the contrary, the laser beam does have a square cross section, and therefore the most likely candidate responsible for the significant colorization of the filamentary structure in the black dashed box is the transmitted laser beam. In addition, the  $25\ \mu\text{m}$  thick Al foil is completely opaque to laser light but almost transparent to energetic ions, electrons, and x-rays. The clear area covered by the  $25\ \mu\text{m}$  thick Al foil indicated by the irregular blue polygon in Fig. 9(c) further confirms that it is the transmitted laser beam that is responsible for the significant colorization of the filamentary structure. In Fig. 9(c), it is notable that the black dashed square is more than twice the size of the red dashed square and that the colorization has a significant filamentary structure. From these features, we suggest that the laser transmission is due to relativistic transparency. Under this hypothesis, the relativistic transparency occurs only in the central area of the laser focus, where the laser intensity exceeds the relativistic transparency threshold, and so the transparent area is smaller than the initial laser focus. The smaller equivalent focus of the transmitted laser leads to a cross section that is larger than the expected laser beam cross section in vacuum. The filamentary structure results from the significant filamentation of the transmitted laser as it passes through the dense plasma. The colorization is much smoother within the purple square at the top of Fig. 9(c). The colorization in this area is considered to be the response of the RCF to energetic ions, electrons, and x-rays and has been taken as the constant background during the calculation of the transmitted laser flux. The results show that the transmittance for the 20 nm CH target is about 25% in Fig. 9(c).

The laser intensity in the experiment was up to  $5 \times 10^{20}\ \text{W}/\text{cm}^2$ , and the corresponding relativistic critical density is  $16n_c$ , which is much less than the initial target electron density. No relativistic transparency should be observed if the target expansion does not occur before the main pulse arrives at the target surface. However, significant expansion of the ultrathin foil by the laser prepulse does occur. A hydrodynamic simulation of this expansion has been carried out with the MULTI-1D code. The simulated profile of the preplasma



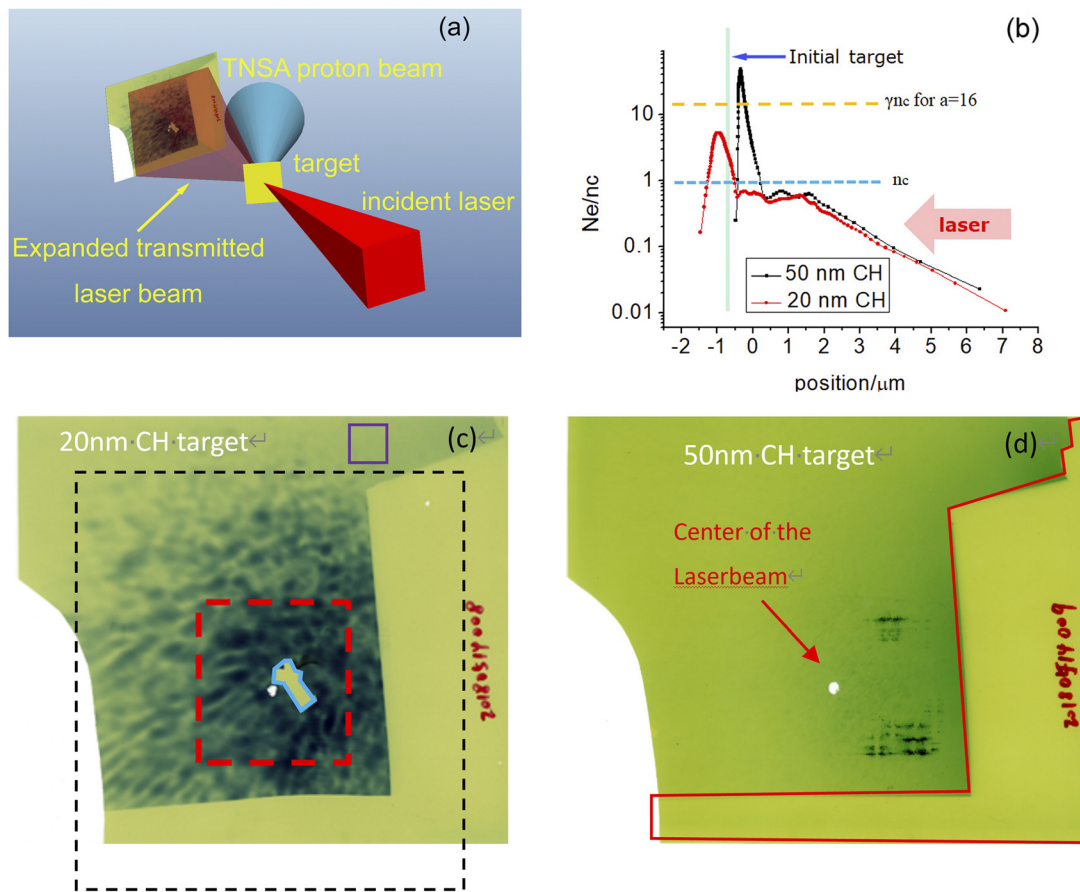


**FIG. 9.** Laser transmission measurement in laser-ultrathin foil interaction. (a) Schematic of experimental setup. (b) Hydrodynamic simulation results for the preplasma profile driven by the laser prepulse, with the intensity of the latter being calculated by taking into account both the actual laser contrast profile and the energy concentrations in the laser spot. (c) and (d) Transmitted laser beams measured by the RCF for 20 nm thick and 50 nm thick plastic foils, respectively. In (c), the purple square in (c) indicates the area where the colorization of RCF was only from the radiation background, the black dashed square indicates the area where the colorization of the RCF was dominated by the transmitted laser beam, the red dashed square indicates the expected laser beam when the laser propagates in vacuum, and the irregular blue polygon indicates the area where the RCF was covered by a  $25\ \mu\text{m}$  thick Al foil, completely blocking the transmitted laser (in some other shots, when  $2\text{--}3\ \mu\text{m}$  thick foils were used, similar blocking of radiation was observed). In (d), the irregular red polygon indicates the area where the RCF was blocked by other installed instruments.

density is shown in Fig. 9(b). For the 50 nm CH foil, the simulation shows the peak preplasma density to be about  $50n_c$ . The thickness when the plasma density exceeds  $16n_c$  is 210 nm, and no transparency should be observed even when the relativistic effect is included. On the other hand, for the 20 nm CH foil, the simulation shows the peak preplasma density to be about  $5.2n_c$ , which is less than the relativistic critical density but still larger than the critical density. These simulation results support the relativistic transparency hypothesis with respect to the observed 25% transmittance for the 20 nm CH target shown in Fig. 9(c).

Table I summarizes experimental transmission results for ultrathin foil targets of different materials and thicknesses, with different laser incident angles. The results reveal the stable operation of the laser with high contrast. The burn-through thickness is between 20 and 50 nm for CH targets when the S-polarized laser is incident on the target at  $30^\circ$ .

### 3. Experimental results related to laser intensity

There is no well-established method for accurately determining the on-target laser intensity by measuring a single physical quantity in the laser interaction. In the commissioning experiment, the laser intensity was estimated by measuring the hot-electron temperature in the laser direction. Generally, the hot electron temperature is related to both the laser intensity and the scale length of the preplasma in the laser-solid target interaction. Because of the high laser contrast of SILEX-II, the scale length is quite short ( $0.35\ \mu\text{m}$ ). Under this condition, the  $\mathbf{J} \times \mathbf{B}$  heating is the main mechanism of hot-electron generation.

The scaling of the hot-electron temperature from the laser intensity in laser interaction with solids has been studied previously.<sup>18–23</sup> According to numerical results from particle-in-cell (PIC) simulations, a ponderomotive scaling model  $T_{\text{hot,pond}} = (1 + a_0^2)^{1/2} - 1$  was suggested by Wilks *et al.*<sup>18</sup> However, this scaling law tends to overestimate the

**TABLE I.** Summary of burn-through measurements of nanometer-thick foil targets under different experimental conditions.

Material	Thickness (nm)	Transmission probability for incidence angle 30°	Transmission probability for normal incidence
SiN	50		0/3
	20		
CH	50	0/2	1/4
	20	2/2	

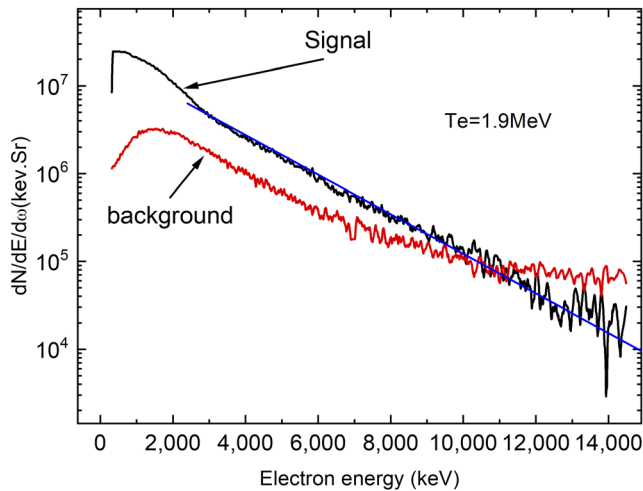


**FIG. 10.** Measured hot-electron spectra in the laser direction for a 2 μm thick copper foil.

hot-electron temperature when compared with experiments. For example, the experiments by Beg *et al.*<sup>19</sup> at intensities ranging from  $3 \times 10^{16}$  to  $6 \times 10^{18}$  W/cm<sup>2</sup> indicate that the hot-electron temperature is given by a one-third power-law scaling  $T_h$  (keV) = 215  $(I_{18} \lambda_{\mu\text{m}}^2)^{1/2}$ , which is a much weaker scaling than that given by the ponderomotive model. More recent experiments<sup>20,21</sup> confirm that this one-third scaling extends to high laser intensities of  $10^{19-21}$  W/cm<sup>2</sup>. To explain the weaker electron temperature scaling, a relativistic model based on energy and momentum conservation laws was proposed by Haines *et al.*,<sup>22</sup> giving  $T_e(m_e c^2) = (1 + 2^{1/2} a_0)^{1/2} - 1$ . It was shown that the hot-electron temperature given by the scaling law of Haines *et al.* agrees with the

experimental scaling of Beg *et al.* for a wide range of laser intensities. Kluge *et al.*<sup>23</sup> proposed another analytical model that focuses on the ensemble dynamics at the critical density interface by taking into account the distribution of electrons with respect to the laser phase. This novel approach makes it possible to accurately predict the scaling of hot-electron temperature seen in experiments and simulations for both nonrelativistic and relativistic intensities. For  $a_0 \gg 1$ , the model of Kluge *et al.* gives  $T_e^h(m_e c^2) = \pi a_0 / (2 \ln 16 + 2 \ln a_0) - 1$ . This scaling converges with that of Haines *et al.* for moderate laser intensities in the range  $a_0 = 1-20$ , while it predicts much higher electron temperatures than the Haines *et al.* scaling for high laser intensities  $a_0 > 20$ . Thus, in the present experiment with laser intensities around  $10^{20-21}$  W/cm<sup>2</sup>, both the Haines *et al.* and Kluge *et al.* scaling laws are appropriate and can be used to estimate the on-target laser intensities from the measurement of hot electron temperature.

The typical hot-electron spectrum of a mono-temperature structure in the laser propagation direction when a 2 μm thick copper foil is used as the target is shown in Fig. 10. The fitted temperature is 1.9 MeV for the hot electrons whose energy is more than 3 MeV. According to the theoretical scaling law of Haines *et al.*, the corresponding laser intensity is  $4.9 \times 10^{20}$  W/cm<sup>2</sup>.<sup>22-25</sup> The calculated intensity is  $4.7 \times 10^{20}$  W/cm<sup>2</sup>, based on the 31 J laser energy and 31 fs laser pulse duration of this shot. The difference in laser intensity between the two approaches is 4%. A comparison of the laser intensity between the two approaches for three shots is summarized in Table II. The difference is within 20%. The experimental results show that the scaling law of Haines *et al.* is valid in our experiments and that the maximum laser intensity is about  $5 \times 10^{20}$  W/cm<sup>2</sup>.

### C. Laser proton acceleration

Laser proton acceleration is one of the important applications of intense ultra-short-pulse lasers.<sup>26,27</sup> The acceleration is related to the

**TABLE II.** Comparison of laser intensities measured by two approaches:  $I_{\text{laser}}$  is from measured laser parameters, and  $I_{Te}$  is from the scaling law of Haines *et al.* and the experimental hot-electron temperature.

Shot No.	Laser energy (J)	Pulse duration (fs)	Laser intensity from laser parameter measurement, $I_{\text{laser}}$ ( $10^{20}$ W/cm <sup>2</sup> )	Laser intensity from hot-electron temperature measurement and using Haines <i>et al.</i> scaling law		Ratio $I_{\text{laser}}/I_{Te}$
				Laser intensity $I_{Te}$ ( $10^{20}$ W/cm <sup>2</sup> )	$T_e$ (MeV)	
t004	31	31	4.7	4.9	1.9	0.96
005	29.8	35	4.0	3.4	1.7	1.18
t006	18.3	29	3.0	2.6	1.57	1.14



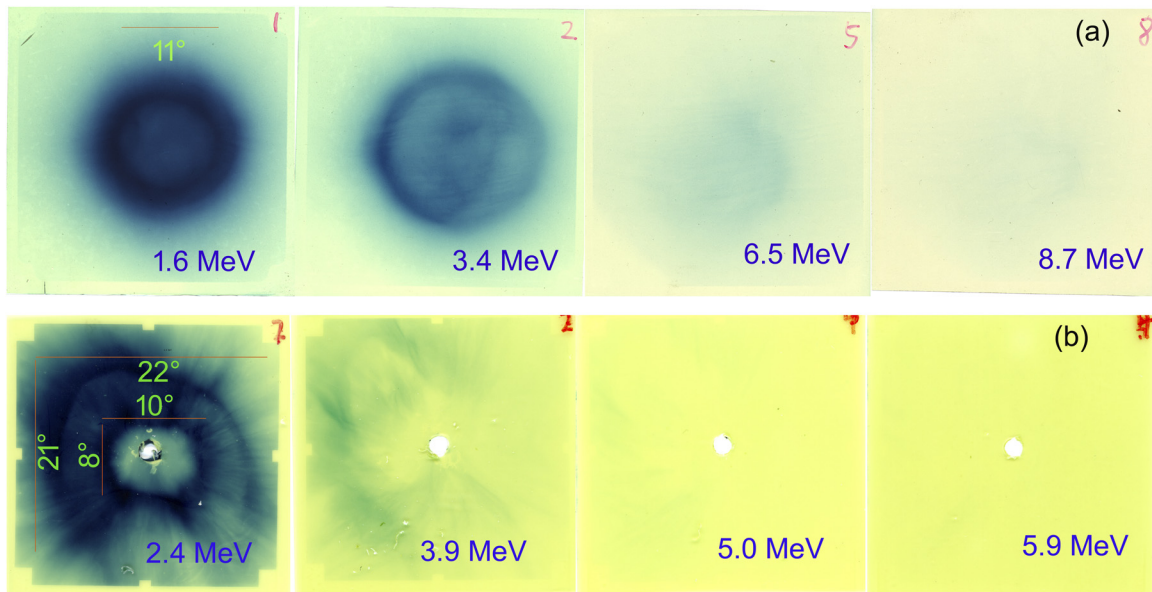


FIG. 11. Proton beam profile measured with RCF (HD-V2) stack in the normal direction of the target rear side for different foils: (a) 7  $\mu\text{m}$  copper foil; (b) 10 nm C foil.

laser intensity, pulse duration, contrast ratio, and laser polarization. The maximum proton energy achievable is one of the important measures of a laser facility’s capabilities.

Proton acceleration mechanisms include TNSA,<sup>28–30</sup> radiation-pressure-dominated acceleration (RPDA),<sup>31,32</sup> and transparency-enhanced hybrid acceleration.<sup>33</sup> The dominant acceleration mechanism in an experiment is determined by the laser and target parameters. We systematically changed the target thickness while the S-polarized laser was incident on the foils at 30°. The target thickness changed from 10 nm to 15  $\mu\text{m}$ . The main target material was copper, but CH, SiN, and carbon foils were used when the target thickness was less than 200 nm.

Typical proton beams measured with an RCF stack are shown in Fig. 11(a) for a target thickness greater than 200 nm and in Fig. 11(b) for a target thickness less than 200 nm. In Fig. 10(a), the target is 7  $\mu\text{m}$  thick copper foil, and the maximum proton energy is 13 MeV. A prominent ring-like structure is present for low-energy protons. The full divergent angle is as small as 11° for 1.6 MeV protons, which indicates the high laser contrast. In Fig. 10(b), the target is 10 nm thick C foil, and the maximum proton energy is 5.9 MeV. A double-ring-like structure is clearly present for 2.4 MeV protons. The full divergent angles in the horizontal direction for the inner and outer rings are 10° and 22°, respectively.

The dependence of the maximum proton energy on target thickness is shown in Fig. 12. The maximum proton energy is roughly independent of target thickness when no significant laser transmission occurs. The average proton energy is 14 MeV, and the maximum is 21 MeV. The average proton energy decreases to about 7 MeV owing to the weaker laser absorption when significant laser transmission occurs. Similar results for the dependence of proton energy on target thickness<sup>34–36</sup> and of proton beam profile on target thickness<sup>37,38</sup> have been reported in the literature. Under the present experimental conditions, TNSA is suggested to be the dominant mechanism of proton

acceleration. It is well known that if the laser irradiance is extremely high, radiation pressure can bring about another very efficient acceleration mechanism, namely RPDA.<sup>31</sup> In general, the RPDA can be achieved for laser intensities  $>10^{21}$  W/cm<sup>2</sup> with preferred conditions of circular polarization, normal incidence, and ultra-high laser contrast. For the present experiments, however, the incident laser has an intensity of about  $5 \times 10^{20}$  W/cm<sup>2</sup> with S-polarization. More importantly, although the laser contrast is as high as  $10^{10}$ , a preplasma with a scale length of 0.35  $\mu\text{m}$  is still formed before the arrival of the main laser pulse. This preplasma can enhance the laser absorption and subsequent hot-

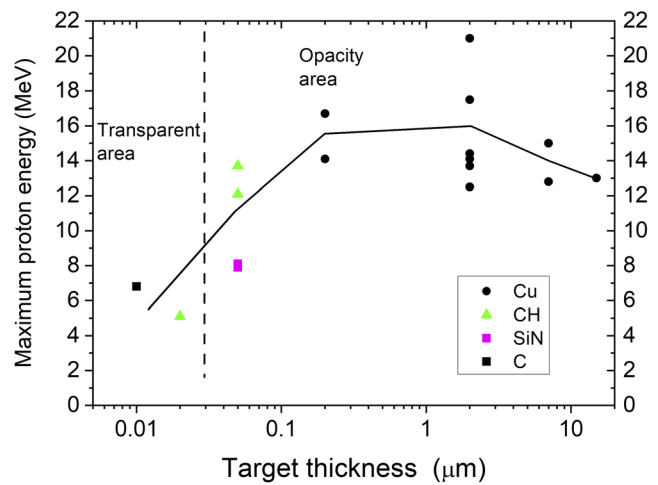


FIG. 12. Effect of target thickness on maximum proton energy in the target normal direction.

electron generation, thus reinforcing the electric sheath field on the target rear side, which comes to dominate the proton acceleration. Therefore, under the present experimental conditions, the most energetic protons come from the target rear side by TNSA instead of from the target front surface by RPDA. Also, in the case of TNSA, the electron reflux effect is expected to play an important role in the proton acceleration, depending on the target thickness.<sup>39</sup> This is confirmed by the experimental results. As can be seen in Fig. 12, the maximum proton energy decreases with increasing target thickness when the latter is greater than  $2\ \mu\text{m}$ . This decrease in proton energies with thicker targets can thus be partially interpreted as the result of the reduced electron reflux effect.

#### IV. CONCLUSIONS

A commissioning experiment has been carried out on the high-contrast petawatt-class complete OPCPA SILEX-II laser facility. The experimental results show that the maximum laser intensity is about  $5 \times 10^{20}\ \text{W}/\text{cm}^2$  within a  $5.8\ \mu\text{m}$  focus (FWHM) and that the performance of the laser is relatively stable. Although  $50\ \text{nm}$  thick CH foils were not burned through by the laser prepulse, significant laser transmission was observed for  $20\ \text{nm}$  thick CH foils.

The on-target laser power of the SILEX-II laser facility is to be increased to  $3\ \text{PW}$  and the laser intensity will go beyond  $1 \times 10^{21}\ \text{W}/\text{cm}^2$ . The current laser focus quality is far from the best achievable and will be improved constantly. The laser intensity should be able to reach  $1 \times 10^{22}\ \text{W}/\text{cm}^2$  if the laser focus is decreased to  $2\ \mu\text{m}$  and the concentration increased by a factor of two. To further improve the laser contrast, it should be easy to set up a traditional plasma mirror for this laser facility, thanks to its high intrinsic contrast. Furthermore, an ellipsoidal plasma mirror<sup>40,41</sup> would be a better option to achieve simultaneously higher intensity and better laser contrast.

#### ACKNOWLEDGMENTS

This work was supported by the National Key Program for S&T Research and Development (Grant No. 2018YFA0404804), the Science Challenge Project (Grant No. TZ2016005), and the National Natural Science Foundation of China (Grant No. 11805181).

#### AUTHOR DECLARATIONS

##### Conflict of Interest

The authors have no conflicts to disclose.

#### REFERENCES

- <sup>1</sup>D. Strickland and G. Mourou, "Compression of amplified chirped optical pulses," *Opt. Commun.* **56**(3), 219–221 (1985).
- <sup>2</sup>C. Danson, D. Hillier, N. Hopps *et al.*, "Petawatt class lasers worldwide," *High Power Laser Sci. Eng.* **3**, E3 (2015).
- <sup>3</sup>C. N. Danson, C. Haefner, J. Bromage *et al.*, "Petawatt and exawatt class lasers worldwide," *High Power Laser Sci. Eng.* **7**, E54 (2019).
- <sup>4</sup>H. Kiriya, A. S. Pirozhkov, M. Nishiuchi *et al.*, "High-contrast high-intensity repetitive petawatt laser," *Opt. Lett.* **43**(11), 2595 (2018).
- <sup>5</sup>A. S. Pirozhkov, Y. Fukuda, M. Nishiuchi *et al.*, "Approaching the diffraction-limited, bandwidth-limited Petawatt," *Opt. Express* **25**(17), 20486 (2017).
- <sup>6</sup>W. Li, Z. Gan, L. Yu *et al.*, "339 J high-energy Ti:sapphire chirped-pulse amplifier for 10 PW laser facility," *Opt. Lett.* **43**(22), 5681–5684 (2018).

- <sup>7</sup>A. D. Piazza, K. N. Muller, and K. N. Hatsagortsyan, "Extremely high-intensity laser interactions with fundamental quantum systems," *Rev. Mod. Phys.* **84**(3), 1177 (2012).
- <sup>8</sup>H. S. Peng, W. Y. Zhang, X. M. Zhang *et al.*, "Progress in ICF programs at CAEP," *Laser Part. Beams* **23**(2), 205–209 (2005).
- <sup>9</sup>Z. Qihua, Z. Kainan, S. Jingqin *et al.*, "The Xingguang-III laser facility: Precise synchronization with femtosecond, picosecond and nanosecond beams," *Laser Phys. Lett.* **15**(1), 015301 (2018).
- <sup>10</sup>X. Zeng, K. Zhou, Y. Zuo *et al.*, "Multi-petawatt laser facility fully based on optical parametric chirped-pulse amplification," *Opt. Lett.* **42**(10), 2014–2017 (2017).
- <sup>11</sup>K. Zhou, X. Huang, X. Zeng *et al.*, "Improvement of focusing performance for a multi-petawatt OPCPA laser facility," *Laser Phys.* **28**, 125301 (2018).
- <sup>12</sup>J. Kern, S. Feldman, I. Kim *et al.*, "Simultaneous imaging of K- $\alpha$  radiation and coherent transition radiation from relativistic-intensity laser-irradiated solid target plasmas," *High Energy Density Phys.* **8**(1), 60–65 (2012).
- <sup>13</sup>J. Zheng, K. A. Tanaka, T. Sato *et al.*, "Study of hot electrons by measurement of optical emission from the rear surface of a metallic foil irradiated with ultraintense laser pulse," *Phys. Rev. Lett.* **92**(16), 165001 (2004).
- <sup>14</sup>G.-Q. Liao, Y.-T. Li, Y.-H. Zhang *et al.*, "Demonstration of coherent terahertz transition radiation from relativistic laser-solid interactions," *Phys. Rev. Lett.* **116**(20), 205003 (2016).
- <sup>15</sup>Y. Glinec, J. Faure, A. Norlin *et al.*, "Observation of fine structures in laser-driven electron beams using coherent transition radiation," *Phys. Rev. Lett.* **98**(19), 194801 (2007).
- <sup>16</sup>L. Veisz, W. Theobald, T. Feurer *et al.*, "Three-halves harmonic emission from femtosecond laser produced plasmas with steep density gradients," *Phys. Plasmas* **11**, 3311 (2004).
- <sup>17</sup>Y. He, W. Hong, J. Hua *et al.*, "Measuring fluence distribution of intense short laser based on the radiochromic effect," *Opt. Lett.* **46**(11), 2795–2798 (2021).
- <sup>18</sup>S. C. Wilks, W. L. Kruer, M. Tabak *et al.*, "Absorption of ultra-intense laser pulses," *Phys. Rev. Lett.* **69**(9), 1383 (1992).
- <sup>19</sup>F. N. Beg, A. R. Bell, A. E. Dangor *et al.*, "A study of picosecond laser-solid interactions up to  $10^{19}\ \text{W cm}^{-2}$ ," *Phys. Plasmas* **4**(2), 447–457 (1997).
- <sup>20</sup>C. D. Chen, P. K. Patel, D. S. Hey *et al.*, "Bremsstrahlung and K $\alpha$  fluorescence measurements for inferring conversion efficiencies into fast ignition relevant hot electrons," *Phys. Plasmas* **16**(8), 082705 (2009).
- <sup>21</sup>H. Chen, S. C. Wilks, W. L. Kruer *et al.*, "Hot electron energy distributions from ultraintense laser solid interactions," *Phys. Plasmas* **16**(2), 020705 (2009).
- <sup>22</sup>M. G. Haines, M. S. Wei, F. N. Beg *et al.*, "Hot-electron temperature and laser-light absorption in fast ignition," *Phys. Rev. Lett.* **102**(4), 045008 (2009).
- <sup>23</sup>T. Kluge, T. Cowan, A. Debus *et al.*, "Electron temperature scaling in laser interaction with solids," *Phys. Rev. Lett.* **107**(20), 205003 (2011).
- <sup>24</sup>M. Sherlock, "Universal scaling of the electron distribution function in one-dimensional simulations of relativistic laser-plasma interactions," *Phys. Plasmas* **16**(10), 103101 (2009).
- <sup>25</sup>A. J. Kemp, Y. Sentoku, and M. Tabak, "Hot-electron energy coupling in ultraintense laser-matter interaction," *Phys. Rev. E* **79**(6), 066406 (2009).
- <sup>26</sup>H. Daido, M. Nishiuchi, and A. S. Pirozhkov, "Review of laser-driven ion sources and their applications," *Rep. Prog. Phys.* **75**(5), 056401 (2012).
- <sup>27</sup>A. Macchi, M. Borghesi, and M. Passoni, "Ion acceleration by superintense laser-plasma interaction," *Rev. Mod. Phys.* **85**(2), 751–793 (2013).
- <sup>28</sup>S. C. Wilks, A. B. Langdon, T. E. Cowan *et al.*, "Energetic proton generation in ultra-intense laser-solid interactions," *Phys. Plasmas* **8**(2), 542 (2001).
- <sup>29</sup>R. A. Snavely, M. H. Key, S. P. Hatchett *et al.*, "Intense high-energy proton beams from petawatt-laser irradiation of solids," *Phys. Rev. Lett.* **85**(14), 2945–2948 (2000).
- <sup>30</sup>P. Mora, "Thin-foil expansion into a vacuum," *Phys. Rev. E* **72**(5), 056401 (2005).
- <sup>31</sup>A. P. L. Robinson, M. Zepf, S. Kar *et al.*, "Radiation pressure acceleration of thin foils with circularly polarized laser pulses," *New J. Phys.* **10**(1), 013021 (2008).
- <sup>32</sup>T. Esirkepov, M. Borghesi, S. V. Bulanov *et al.*, "Highly efficient relativistic-ion generation in the laser-piston regime," *Phys. Rev. Lett.* **92**(17), 175003 (2004).
- <sup>33</sup>A. Higginson, R. J. Gray, M. King *et al.*, "Near-100 MeV protons via a laser-driven transparency-enhanced hybrid acceleration scheme," *Nat. Commun.* **9**, 724 (2018).

- <sup>34</sup>P. L. Poole, L. Obst, G. E. Cochran *et al.*, “Laser-driven ion acceleration via target normal sheath acceleration in the relativistic transparency regime,” *New J. Phys.* **20**, 013019 (2018).
- <sup>35</sup>R. Prasad, A. A. Andreev, D. Doria *et al.*, “Fast ion acceleration from thin foils irradiated by ultra-high intensity, ultra-high contrast laser pulses,” *Appl. Phys. Lett.* **99**, 121504 (2011).
- <sup>36</sup>R. Prasad, S. Ter-Avetisyan, D. Doria *et al.*, “Proton acceleration using 50 fs, high intensity ASTRA-Gemini laser pulses,” *Nucl. Instrum. Methods Phys. Res., Sect. A* **653**(1), 113–115 (2011).
- <sup>37</sup>S. Gaillard, J. Fuchs, N. Renard-Le Galloudec *et al.*, “Study of saturation of CR39 nuclear track detectors at high ion fluence and of associated artifact patterns,” *Rev. Sci. Instrum.* **78**(1), 013304 (2007).
- <sup>38</sup>G. A. Becker, S. Tietze, S. Keppler *et al.*, “Ring-like spatial distribution of laser accelerated protons in the ultra-high-contrast TNSA-regime,” *Plasma Phys. Controlled Fusion* **60**(5), 055010 (2018).
- <sup>39</sup>A. J. Mackinnon, Y. Sentoku, P. K. Patel *et al.*, “Enhancement of proton acceleration by hot-electron recirculation in thin foils irradiated by ultraintense laser pulses,” *Phys. Rev. Lett.* **88**(21), 215006 (2002).
- <sup>40</sup>D. Kumar, M. Smid, S. Singh *et al.*, “Alignment of solid targets under extreme tight focus conditions generated by an ellipsoidal plasma mirror,” *Matter Radiat. Extremes* **4**(2), 024402 (2019).
- <sup>41</sup>M. Nakatsutsumi, A. Kon, S. Buffechoux *et al.*, “Fast focusing of short-pulse lasers by innovative plasma optics toward extreme intensity,” *Opt. Lett.* **35**(13), 2314–2316 (2010).